Available online at www.sciencedirect.com

ScienceDirect

(Submitted to AMC, Sept, 2022) 00 (2023) 1–21

Journal Logo

Image Segmentation Based on the Hybrid Bias Field Correction

Zhi-Feng Pang[†,*], Zhenyan Guan[†], Yue Li[†], Ke Chen[‡], and Hong Ge[§]

[†]College of Mathematics and Statistics, Henan University, Kaifeng, 475004, Henan Province, China.

[‡] Department of Mathematical Sciences, University of Liverpool, Liverpool, L69 7ZL, UK.

[§] Department of Radiation Oncology, The Affiliated Cancer Hospital of Zhengzhou University, Zhengzhou 450008, China.

Abstract

Image segmentation is the foundation for analyzing and understanding high-level images. How to effectively segment the intensity inhomogeneous image into several meaningful regions in terms of human visual perception and ensure that the segmented regions are consistent at different resolutions is still a very challenging task. In order to describe the structure information of the intensity inhomogeneous efficiently, this paper proposes a novel hybrid bias field correction model by decoupling the multiplicative bias field and the additive bias field. Since these kinds of bias fields are assumed to be smooth, we can employ the Sobolev space $W^{1,2}$ to feature them and use a constraint to the multiplicative bias field. Since the proposed model is a constrained optimization problem, we use the Lagrangian multiplier method to transform it into an unconstrained optimization problem, and then the alternating direction method can be used to solve it. In addition, we also discuss some mathematical properties of our proposed model and algorithm. Numerical experiments on the natural images and the medical images demonstrate performance improvement over several state-of-the-art models.

Keywords: Image segmentation, Intensity inhomogeneity, Multiplicative bias field, Additive bias field, Alternating direction method

1. Introduction

During the past decades, there has been a lot of studies on image segmentation[23, 24, 28, 38, 46]. Various deep learning-based methods and variational-PDE methods have been proposed for image segmentation [12, 32, 40, 50]. In the learning-based methods, although the segmentation algorithm has made great progress, there are still problems such as lack of interpretability, insufficient feature extraction ability, loss of detailed information, and low segmentation efficiency, which cannot meet the requirements of image segmentation. Especially, learning-based methods lack a theoretical foundation and rely heavily on massive labeled data. In addition, these methods rarely consider the image priors existing in statistical and structural information. The variational partial differential equation (PDE) methods are usually constructed based on Bayesian maximum a posteriori (MAP) estimation. To be more specific, the variational PDE methods regard the segmentation processing as an ill-posed inverse problem and construct the energy function according to the segmentation target between the segmentation regions and the segmentation curves. These methods generally include region-based models, edge-based models and their hybridization. Region-based segmentation methods utilize region information to guide the evolution of initial contours. Chan-Vese (CV) model [6], Local Binary

Email address: zhifengpang@163.com, guanzhenyan0925@163.com; liyue7278@163.com; k.chen@liverpool.ac.uk; gehong666@126.com. (*Corresponding author) (Zhi-Feng Pang[†,*], Zhenyan Guan[†], Yue Li[†], Ke Chen[‡], and Hong Ge[§])

Fitted (LBF) model [18] and Local Intensity Clustering (LIC) model [16] are the approaches of region-based models. In edge-based segmentation methods, the segmentation process is performed by evolving the initial contour to the target boundary such as Snake model [15], Geodesic active contours model [5]. However, the edge-based methods are greatly affected by the initial contour and the boundary of the target object, and curve evolution tends to fall to a local minimum. Furthermore, the edge-based models are usually required to assume that the gray distribution is uniform. Therefore, they cannot achieve a good segmentation effect for images with intensity inhomogeneity or noise. In fact, it is a challenging task to segment regions of interest from images with inhomogeneous intensity since the inhomogeneous intensity weak the image edge. To this end, many efforts have been done on the problem of image segmentation with inhomogeneous intensity [2, 7, 17, 33].

Intensity inhomogeneity is present in many real-world images from different modalities, such as X-ray/tomography, magnetic resonance images and some natural images. Intensity inhomogeneity is a smoothly varying bias field. For instance, in magnetic resonance imaging (MRI), intensity inhomogeneity can lead to inconsistency of pixels in the same tissue [35]. This phenomenon also occurs in natural images, mostly due to uneven lighting [14]. To deal with the image segmentation problem of intensity inhomogeneity, Chan and Vese [36] proposed a piecewise smooth (PS) model. This method used the piecewise smooth function to replace the constant value function, and effectively segment the image with intensity inhomogeneity. However, this model requires periodic initialization when using the level set method to solve it, which is difficult to apply and cannot be generalized. Furthermore, the solution can easily get stuck in local minima due to the non-convexity of the model and then the model heavily depends on the choice of the initialization. Li et al. [18] introduced the kernel function to the active contour model and then proposed the local binary fitting (LBF) model to drive the evolution of the curve, and at the same time added a penalty term to the energy function to avoid the problem of level set re-initialization. The LBF model is sensitive to the initial contour because it does not contain any global information about the image. In the literature [16], Li et al. proposed a local intensity clustering (LIC) model to complete the bias field correction by introducing a bias field into the segmentation model and then improving the dependence on the initial contour of the proposed model. For the image with different degrees of gray heterogeneity and noise, the LIC model can produce obvious deficiencies. In the literature [11], Gao et al. introduced a locally modified CV model to handle images with uneven intensity. However, this model is not robust for images with severe intensity inhomogeneity or noise. Zhang et al.[48] proposed a novel level set method to model inhomogeneous objects as Gaussian distributions with different means and variances, and used sliding windows to map the original image to another domain, which is used in image segmentation with uneven intensity. Although this approach has produced impressive results, it has the disadvantage of utilizing restricted local information, which might weaken the anti-noise ability. Duan et al. [8] introduced an L_0 gradient regularizer to model the true intensity and a smooth regularizer to model the bias field. Although the model performed well for images with uneven intensity and can obtain intensity-corrected (uniform) images, some details may be lost due to the logarithmic transformation. Ali et al. [1] proposed a variation-based model from multiplicative and difference images to handle intensity inhomogeneity, which turned out to outperform the CV model and its many variants. Subudhi et al. [34] proposed a fuzzy set based on Gibbs Markov random field to model the spatial background information of magnetic resonance imaging and combined it with the principle of maximum posterior probability estimation to segment images with uneven illumination. The model used the fuzzy set theory framework to solve the problem of bias field effects in MRI images. Memon et al. [27] proposed a region-based hybrid active contour model, where the weight function can obtain smooth contour boundaries at different intensity levels and suppress the evolution of false contours and regularize the target boundaries. However, these local region-based active contour models (ACMs) were sensitive to the initial position, and an improper initial curve led to poor segmentation results.

Different from the above-mentioned model which either assumes that the image is decomposed as the product of the smooth image and the piecewise constant image[20, 28, 34, 48] or assumes that the image is the sum of the smooth image and the piecewise constant image[8, 13, 25, 41, 50], this paper proposes a new hybrid model by coupling with some advantages between the multiplicative bias field correction and the additive bias field correction for segmenting the intensity inhomogeneous images. Since these bias fields are assumed to be smooth, we use the Sobolev space $W^{1,2}$ to describe them. In addition, we add a constraint for the multiplicative bias field to make it slowly change within a certain range. Since our proposed model can be transformed into a non-smooth optimization, the alternating direction method can be then used to solve it and some good mathematical properties of the algorithm and model are effectively maintained. Extensive experiments on natural images and medical images from some benchmark datasets show that the proposed segmentation model outperforms several state-of-the-art methods in terms of robustness to the segmentation accuracy.

The framework of this paper is as follows: Section 2 mainly introduces the multiplicative bias field model and the additive bias field model, which are closely related to the motivation of our proposed model. Section 3 gives our proposed hybrid bias field correction model and an efficient numerical algorithm is proposed to solve the proposed model. Moreover, we show the existence and convergence analysis of the solution. To show the robustness of our proposed model compared with several state-of-the-art methods, Section 4 presents some numerical comparisons for dealing with the natural images and the medical images. Finally, conclusions of this work are drawn in Section 5.

Notations

Throughout this paper, let $\Omega \subset \mathbb{R}^2$ be an open and bounded image domain, and $I : \Omega \to \mathbb{R}$ be an observed grayscale image to be segmented. Let C be the edge set in Ω. The purpose of segmentation is to divide the image domain Ω into two disjoint parts $\{\Omega_i\}_{i=1}^2$, such that $\Omega = \Omega_1 \cup \Omega_2 \cup C$. i.e. $\Omega_1 \cap \Omega_2 = \emptyset$.

2. Related Works

In this section, several previous works closely related to our proposed framework are reviewed. To segment the intensity inhomogeneous image, the main challenge is to remove the bias field and then require the processed image to be piecewise constant. These methods can be summarized into two kinds as the multiplicative bias field methods and the additive bias field methods.

2.1. Multiplicative bias field methods

The multiplicative bias field methods can be modeled by the Retinex theory [21, 42]. According to the basic idea of the Retinex model, an image can be represented as the product of the illuminance component and reflection component. More specifically, the illuminance component corresponds to the smooth image and the reflection component corresponds to the piecewise constant image. Based on the Retinex theory, the intensity of inhomogeneous image I can be modeled by

$$I = \hat{b}J_1 + n, \tag{1}$$

where the illuminance component J_1 represents the intrinsic physical characteristics of the observed image, n is the zero-mean Gaussian noise. The reflection component $\hat{b}$ denotes the bias field, i.e., uneven intensity. Li et al.[20] proposed multiplicative intrinsic component optimization (MICO) model for bias field estimation and segmentation of magnetic resonance (MR) images. This model considered the bias field $\hat{b}$ and the true piecewise constant image J_1 as the multiplicative intrinsic components of an observed image. The expression for the two-phase segmentation model is as follows

$$\min_{c_1,c_2,\hat{b},u\in[0,1]} \lambda \int_\Omega (I - \hat{b}c_1)^2 u + (I - \hat{b}c_2)^2(1-u)\mathrm{d}x + \int_\Omega |\nabla u|\mathrm{d}x, \tag{2}$$

where λ is the constant parameter. The bias field $\hat{b}$ is represented by a linear combination of a given set of smooth basis functions $\mathbf{g} = (g_1, \cdots, g_M)^T$. The estimation of the bias field is performed by finding the optimal coefficients $\mathbf{w} = (w_1, \cdots, w_M)^T$ in the linear combination $\hat{b} = \mathbf{w}^T\mathbf{g} = \sum_{k=1}^M w_k g_k$. Here $w_i = (\int_\Omega \mathbf{g}\mathbf{g}^T\mathbf{a}\mathrm{d}x)^{-1}\int_\Omega g_i I\mathbf{a}\ \mathrm{d}x$ for $\mathbf{a} = c_1^2 u + c_2^2(1-u)$ and $i = 1, 2\cdots, M$. The main thought of basis functions can be found in references [20, 29].

2.2. Additive bias field methods

Different from the multiplicative bias field methods, some researchers considered to decompose the intensity inhomogeneous image into the sum of the piecewise constant component and the smooth component. To be specific, the decomposition can be modeled by

$$I = J_2 + \tilde{b} + n, \tag{3}$$

where J_2 is a piecewise constant approximation of I, and $\tilde{b} : \Omega \to \mathbb{R}$ as smooth function modeling inhomogeneous intensities in the image domain Ω. The assumptions about the real image and bias field can be referred to the model (3). Jung [13] proposed a piecewise-smooth image segmentation model (L1PS) by introducing L_1 data-fidelity term.

This model can effectively deal with the image with intensity inhomogeneity and noise. The L1PS model is a typical model of the summation of the bias field and the piecewise constant. The expression for this model is as follows

$$\min_{c_1,c_2,\tilde{b},u\in[0,1]} \lambda \int_\Omega \left|(I-c_1-\tilde{b})u+(I-c_2-\tilde{b})(1-u)\right| \mathrm{dx} + \alpha \int_\Omega |\nabla\tilde{b}|^2 \mathrm{dx} + \int_\Omega |\nabla u| \mathrm{dx}, \tag{4}$$

where λ and α are constant parameters.

3. Main works

This section first gives our proposed model and also discusses the existence of the solution. Then we give an efficient numerical method to solve the proposed model and analysis the convergence of the used algorithm.

3.1. Our proposed model

In general, the natural image and the medical image generally contain not only a multiplicative bias field but also an additive bias field. In the following, we consider the hybrid bias field correction in terms of the multiplicative bias field and additive bias field as

$$I = b_1 J + b_2 + n, \tag{5}$$

where b_1 and b_2 denote the multiplicative bias field and additive bias field respectively, J denotes the piecewise constant image which needs to be segmented.

To expound this motivation of the decomposition (5), we choose a natural image as shown in the first row of Figure 1 to be the testing image. The decomposition results based on different schemes are shown in the 2-4th rows. In order to show the rationality of our proposed scheme, we select a row of pixels in the first column to plot the gray distribution curve and plot them in the second column. It is obvious that our method tends to be more piecewise constant. In addition, an image is composed of pixels with different gray levels, and the distribution of gray levels in an image is an important feature of that image. The histogram of an image depicts the distribution of gray levels in the image, which can visually show how much of the image is occupied by each gray level. Thus, we also plot the histogram of the first column images. These histograms have two peaks which imply the two phase to be reasonable. For a more detailed observation, the histogram based on our decomposition scheme has the largest class difference, that is to say that the pixel values are mainly distributed around 25 and 255. These facts imply that our scheme is more suitable for getting an efficient segmentation.

In order to propose our segmentation model, some assumptions of bias fields b_1 and b_2 are needed to be arranged.

(1) To the bias fields b_1 and b_2, we assume that they are slowly varying and smoothing and we set $b_1 \in W^{1,2}(\Omega)$ and $b_2 \in W^{1,2}(\Omega)$. Furthermore, we also assume that b_1 changes slowly around 1.

(2) The piecewise constant image J is assumed to be two parts as

$$J := J(\mathrm{x}) = \begin{cases} c_1, & \text{if } \mathrm{x} \in \Omega_1, \\ c_2, & \text{if } \mathrm{x} \in \Omega_2. \end{cases}$$

Here Ω_1 denotes the region of interest (ROI) and Ω_2 denotes the outside region of ROI.

Definition 3.1. *Assumed that $u \in L^1(\Omega)$, the definition of total variation (TV) is defined by*

$$\int_\Omega |Du| := \sup\left\{ \int_\Omega u\mathrm{div}(\phi)\mathrm{dx} | \phi \in C_0^1(\Omega;\mathbb{R}^n), |\phi| \le 1 \right\}.$$

Furthermore, the bounded variation (BV) space is defined by $BV(\Omega) := \left\{u \in L^1(\Omega) | \int_\Omega |Du| < \infty\right\}$.

Lemma 3.1. *Supposed that $u_j \in BV(\Omega)(j = 1, \ldots)$ and $u_j \to u$ in $L^1_{loc}(\Omega)$. Then*

$$\int_\Omega |Du| \le \liminf_{j\to\infty} \int_\Omega |Du_j|.$$

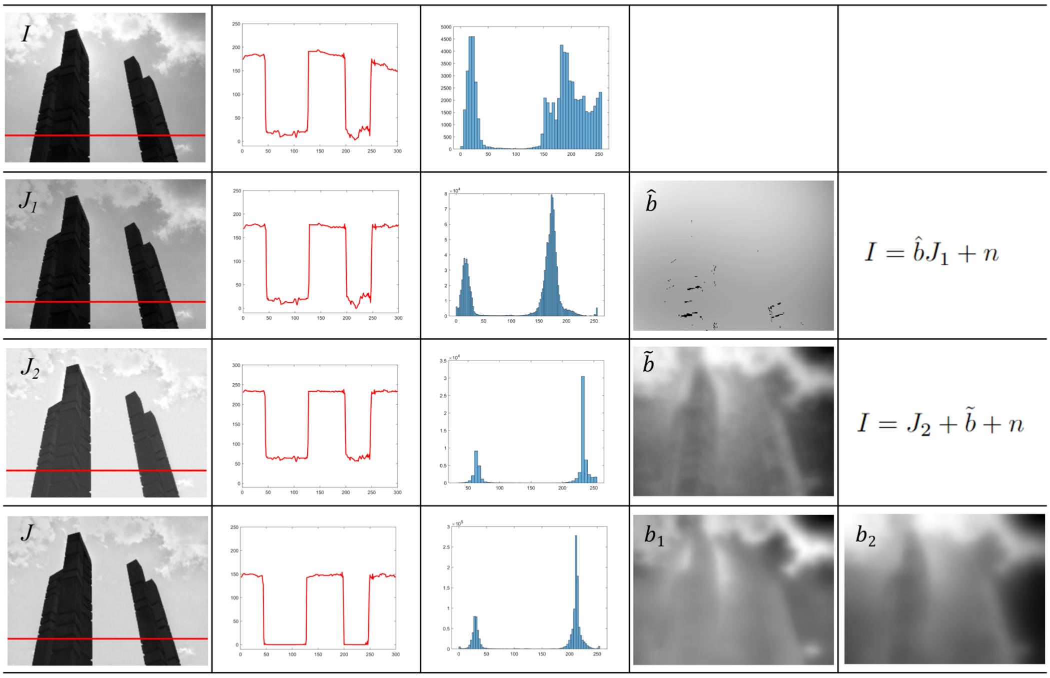

Figure 1. Original image and multiplicative model correction results, additive model correction results, our correction results. Select the 185th row of pixels of the image to display. For the second column, the horizontal coordinate is the horizontal coordinate of the pixel through which the red line passes, and the vertical coordinate is the corresponding gray value. For the third column, the horizontal coordinate is the gray level and the vertical coordinate is the frequency or number of pixels that occur at that gray level.

Remark 3.1. *Based on Definition 3.1, we can deduce that piecewise constant or smooth images are usually assumed in the $BV(\Omega)$ [19]. In addition, we can get $\int_\Omega |Du| = \int_\Omega |\nabla u| \mathrm{dx}$ if u is smooth. In this case, Lemma 3.1 is still satisfied due to the lower semi-continuity of $\int_\Omega |\nabla u| \mathrm{dx}$.*

Based on the above assumptions and Definition 3.1, we propose the following segmentation model

$$\begin{aligned} \min_{u,b_1,b_2,c_1,c_2} \ & \lambda \int_\Omega (I - b_1c_1 - b_2)^2 u + (I - b_1c_2 - b_2)^2(1-u)\mathrm{dx} + \alpha \int_\Omega |\nabla b_1|^2 \mathrm{dx} + \beta \int_\Omega |\nabla b_2|^2 \mathrm{dx} + \int_\Omega |Du|, \\ \text{s.t.} \quad & \int_\Omega (b_1 - 1)^2 \mathrm{dx} \le \varepsilon, \quad u \in \{0, 1\}, \end{aligned} \tag{6}$$

where $\varepsilon > 0$ is the bias parameter, λ, α, β are the weight parameters, and the indicator function u is defined by

$$u := u(\mathrm{x}) = \begin{cases} 1, & \text{if } \mathrm{x} \in \Omega_1, \\ 0, & \text{if } \mathrm{x} \in \Omega_2. \end{cases} \tag{7}$$

Remark 3.2. *On the right side of the model (6), the first term is the data fitting term, which forces $b_1c_i + b_2$ to be close to the input image I for i=1,2, the second term and the third term are smooth term of bias field, which ask that bias fields smoothly. The last term is the length term to regularize the contour. Our goal is to recover $b_i, c_i, i = 1, 2.$ from the observed image I and then obtain the segmentation result. In addition, the bias field b_1 is usually assumed to vary slowly around 1, so we use a constraint term to describe it.*

To the model (6), it is hard to solve numerically due to the binary constraint $u \in \{0, 1\}$. To overcome this drawback, one efficient method is to relax it into a convex set as $u \in [0, 1]$. To the inequality constraint, here we employ the Lagrangian multiplier method. More specifically, we rewrite the model (6) into the following unconstrained optimization problem

$$\min_{u,b_1,b_2,c_1,c_2} E(u,b_1,b_2,c_1,c_2) :=\lambda \int_\Omega (I-b_1c_1-b_2)^2 u + (I-b_1c_2-b_2)^2(1-u)\mathrm{dx} + \alpha \int_\Omega |\nabla b_1|^2 \mathrm{dx} \\ + \beta \int_\Omega |\nabla b_2|^2 \mathrm{dx} + \int_\Omega |\nabla u| \mathrm{dx} + \nu \int_\Omega (b_1-1)^2 \mathrm{dx} + \Gamma_{\mathcal{D}}(u), \tag{8}$$

where $\nu > 0$ is the Lagrangian multiplier and $\Gamma_{\mathcal{D}}(u)$ is defined by

$$\Gamma_{\mathcal{D}}(u) = \begin{cases} 0, & \text{if } u \in \mathcal{D} := [0,1], \\ +\infty, & \text{otherwise.} \end{cases}$$

Now we consider the existence of the solution to the problem (8).

Theorem 3.1. *Define an admissible set* $\Lambda = \{(u,b_1,b_2,c_1,c_2) | u \in BV(\Omega)$ and $u \in \mathcal{D}, b_1, b_2 \in W^{1,2}(\Omega)$, and $0 < c_1, c_2 < P\}$ *for a constant* $P > 0$*. For fixed parameters* $\lambda, \alpha, \beta, \nu$ *are positive, there exists a minimizer* $\left(u^*, b_1^*, b_2^*, c_1^*, c_2^*\right)$ *of problem* (8) *in the admissible set* Λ.

Proof. Since the objective function $E(u,b_1,b_2,c_1,c_2)$ in (8) is positive and proper, its infimum is finite. Then there exists a constant $K > 0$ such that

$$\inf E(u,b_1,b_2,c_1,c_2) \le K. \tag{9}$$

According to the definition of the lower bound, hence there exists a minimizing sequence $\left\{\left(u^\ell, b_1^\ell, b_2^\ell, c_1^\ell, c_2^\ell\right)\right\}$ in Λ such that

$$\lim_{\ell\to\infty} E\left(u^\ell, b_1^\ell, b_2^\ell, c_1^\ell, c_2^\ell\right) = \inf E(u,b_1,b_2,c_1,c_2). \tag{10}$$

Furthermore, we have $\int_\Omega u^\ell \mathrm{dx} \le |\Omega|$ due to $u^\ell \in \mathcal{D}$. By the relative compactness of $BV(\Omega)$ in $L^1(\Omega)$, there exits $u^* \in BV(\Omega)$, such that

$$u^\ell \xrightarrow[L^1(\Omega)]{} u^* \quad \text{and} \quad u^\ell \xrightarrow[\text{a.e. in } \Omega]{} u^*. \tag{11}$$

By the weak lower continuous of the total variation, we have

$$\int_\Omega |\nabla u^*| \mathrm{dx} \le \liminf_{\ell\to\infty} \int_\Omega |\nabla u^\ell| \mathrm{dx}. \tag{12}$$

Now we set $(b_i^\ell)_\Omega := \frac{1}{|\Omega|}\int_\Omega b_i^\ell \mathrm{dx}$ for $i = 1,2$. By the Poincaré inequality [9], it follows that there exist constants $C_1, C_2 > 0$ such that

$$\|b_i^\ell\|_{L^2(\Omega)} = \left\|b_i^\ell - (b_i^\ell)_\Omega\right\|_{L^2(\Omega)} \le C_1 \left\|\nabla b_i^\ell\right\|_{L^2(\Omega)} \le C_2. \tag{13}$$

That is to say that the sequences $\{b_i^\ell\}$ and $\{\nabla b_i^\ell\}$ are bounded in the space $W^{1,2}(\Omega)$. Thus, by the lower semi-continuity, there exists b^* such that

$$\int_\Omega |\nabla b_i^*|^2 \mathrm{dx} \le \liminf_{\ell\to\infty} \int_\Omega |\nabla b_i^\ell|^2 \mathrm{dx}, \quad i = 1,2. \tag{14}$$

and

$$\int_\Omega (b_1^* - 1)^2 \mathrm{dx} = \liminf_{\ell\to\infty} \int_\Omega \left(b_1^\ell - 1\right)^2 \mathrm{dx}. \tag{15}$$

To the sequence $\left\{c_i^\ell\right\}$ with $i = 1,2$, it is bounded in Λ, there then exits a convergent subsequence such that $c_i^\ell \to c_i^*$ as $\ell \to \infty$. According to $u^\ell \to u^*$, $b_i^\ell \to b^*$ and $c_i^\ell \to c_i^*$, based on the Fatou's lemma we get

$$\int_\Omega \liminf_{\ell\to\infty} \left(I - c_1^\ell b_1^\ell - b_2^\ell\right)^2 u^\ell \mathrm{dx} = \int_\Omega \left(I - c_1^* b_1^* - b_2^*\right)^2 u^* \mathrm{dx} \le \liminf_{\ell\to\infty} \int_\Omega \left(I - c_1^\ell b_1^\ell - b_2^\ell\right)^2 u^\ell \mathrm{dx}, \tag{16}$$

$$\int_\Omega \liminf_{\ell\to\infty} \left(I - c_2^\ell b_1^\ell - b_2^\ell\right)^2 u^\ell \mathrm{dx} = \int_\Omega \left(I - c_2^* b_1^* - b_2^*\right)^2 u^* \mathrm{dx} \le \liminf_{\ell\to\infty} \int_\Omega \left(I - c_2^\ell b_1^\ell - b_2^\ell\right)^2 u^\ell \mathrm{dx}. \tag{17}$$

Combining inequalities (12), (14), (15), (16) and (17), we obtain the following inequality

$$E\left(u^*, b_1^*, b_2^*, c_1^*, c_2^*\right) \le \liminf_{\ell\to\infty} E\left(u^\ell, b_1^\ell, b_2^\ell, c_1^\ell, c_2^\ell\right) = \inf E(u,b_1,b_2,c_1,c_2), \tag{18}$$

which proves that $(u^*, b_1^*, b_2^*, c_1^*, c_2^*)$ is a solution of the problem (8). □

3.2. Numerical algorithm

The model (8) is a non-smooth optimization problem due to the term $\int_\Omega |\nabla u| \mathrm{dx}$. The main challenge of the numerical method is how to overcome the non-smoothness. To this end, we first apply the alternating minimization method decouple c_i, b_i with u and then have the following alternating direction scheme

$$
\begin{cases}
(c_1, c_2, b_1, b_2) = \underset{c_1,c_2,b_1,b_2}{\operatorname{argmin}} \ \lambda \int_\Omega (I - b_1 c_1 - b_2)^2 u + (I - b_1 c_2 - b_2)^2 (1-u) \mathrm{dx} \\
\qquad + \alpha \int_\Omega |\nabla b_1|^2 \mathrm{dx} + \beta \int_\Omega |\nabla b_2|^2 \mathrm{dx} + \nu \int_\Omega (b_1 - 1)^2 \mathrm{dx}, & \text{(19a)} \\
u = \underset{u}{\operatorname{argmin}} \ \lambda \int_\Omega \mathcal{S} u \mathrm{dx} + \int_\Omega |\nabla u| \mathrm{dx} + \Gamma_{\mathcal{D}}(u), & \text{(19b)}
\end{cases}
$$

where $\mathcal{S} = (I - b_1 c_1 - b_2)^2 - (I - b_1 c_2 - b_2)^2$.

In the following, we consider how to solve the subproblems (19a) and (19b).

3.2.1. The subproblem (19a)

To the subproblem (c_1, c_2, b_1, b_2), it is non-convex but smooth. To decouple b_1 and b_2 from its optimization condition, we introduce two auxiliary variables and then transform them into the equivalent optimization problem as

$$
\begin{cases}
\underset{c_1,c_2,b_1,b_2}{\min} \ \lambda \int_\Omega p_1^2 u + p_2^2 (1-u) \mathrm{dx} + \alpha \int_\Omega |\nabla b_1|^2 \mathrm{dx} + \beta \int_\Omega |\nabla b_2|^2 \mathrm{dx} + \nu \int_\Omega (b_1 - 1)^2 \mathrm{dx}, \\
\text{s.t.} \quad p_1 = I - b_1 c_1 - b_2, \ p_2 = I - b_1 c_2 - b_2.
\end{cases}
\tag{20}
$$

Based on the augmented Lagrange method, we have the following saddle point problem

$$
\begin{aligned}
\underset{c_1,c_2,b_1,b_2,p_1,p_2}{\min} \ \underset{\xi_1,\xi_2}{\max} \ \mathcal{L}(c_1, c_2, b_1, b_2, p_1, p_2; \xi_1, \xi_2) = {} & \lambda \int_\Omega p_1^2 u + p_2^2 (1-u) \mathrm{dx} \\
& + \alpha \int_\Omega |\nabla b_1|^2 \mathrm{dx} + \beta \int_\Omega |\nabla b_2|^2 \mathrm{dx} + \nu \int_\Omega (b_1 - 1)^2 \mathrm{dx} \\
& - \int_\Omega \xi_1 (p_1 - (I - b_1 c_1 - b_2)) \mathrm{dx} + \frac{r}{2} \int_\Omega (p_1 - (I - b_1 c_1 - b_2))^2 \mathrm{dx} \\
& - \int_\Omega \xi_2 (p_2 - (I - b_1 c_2 - b_2)) \mathrm{dx} + \frac{r}{2} \int_\Omega (p_2 - (I - b_1 c_2 - b_2))^2 \mathrm{dx},
\end{aligned}
$$

where $\mathcal{L}(c_1, c_2, b_1, b_2, p_1, p_2; \xi_1, \xi_2)$ is the augmented Lagrangian function, ξ_1 and ξ_2 are the Lagrange multipliers that can be seen as the dual variables, r represents the penalty parameter. With the help of the alternating direction method of multipliers (ADMM) [22, 31, 37], we can solve the above problem with the Gaussian-Seidel iteration scheme

$$
\begin{cases}
c_1^{k+1} = \underset{c_1}{\operatorname{argmin}} \, \mathcal{L}\left(c_1, c_2^k, b_1^k, b_2^k, p_1^k, p_2^k; \xi_1^k, \xi_2^k\right), & \text{(21a)} \\
c_2^{k+1} = \underset{c_2}{\operatorname{argmin}} \, \mathcal{L}\left(c_1^{k+1}, c_2, b_1^k, b_2^k, p_1^k, p_2^k; \xi_1^k, \xi_2^k\right), & \text{(21b)} \\
b_1^{k+1} = \underset{b_1}{\operatorname{argmin}} \, \mathcal{L}\left(c_1^{k+1}, c_2^{k+1}, b_1, b_2^k, p_1^k, p_2^k; \xi_1^k, \xi_2^k\right), & \text{(21c)} \\
b_2^{k+1} = \underset{b_2}{\operatorname{argmin}} \, \mathcal{L}\left(c_1^{k+1}, c_2^{k+1}, b_1^{k+1}, b_2, p_1^k, p_2^k; \xi_1^k, \xi_2^k\right), & \text{(21d)} \\
p_1^{k+1} = \underset{p_1}{\operatorname{argmin}} \, \mathcal{L}\left(c_1^{k+1}, c_2^{k+1}, b_1^{k+1}, b_2^{k+1}, p_1, p_2^k; \xi_1^k, \xi_2^k\right), & \text{(21e)} \\
p_2^{k+1} = \underset{p_2}{\operatorname{argmin}} \, \mathcal{L}\left(c_1^{k+1}, c_2^{k+1}, b_1^{k+1}, b_2^{k+1}, p_1^{k+1}, p_2; \xi_1^k, \xi_2^k\right), & \text{(21f)} \\
\xi_1^{k+1} = \xi_1^k - r\left(p_1^{k+1} - \left(I - b_1^{k+1} c_1^{k+1} - b_2^{k+1}\right)\right), & \text{(21g)} \\
\xi_2^{k+1} = \xi_2^k - r\left(p_2^{k+1} - \left(I - b_1^{k+1} c_2^{k+1} - b_2^{k+1}\right)\right). & \text{(21h)}
\end{cases}
$$

- *The subproblems* (21a) *and* (21b). These subproblems can be written as

$$c_i^{k+1} \in \arg\min_{c_i} \int_\Omega \left(p_i^k - \left(I - b_1^k c_i - b_2^k\right) - \frac{\xi_i^k}{r} \right)^2 \mathrm{dx}, \tag{22}$$

for $i = 1, 2$. This problem is smooth and the optimal solution can be obtained by

$$c_i^{k+1} = \frac{\int_\Omega b_1^k \left(I - b_2^k - p_i^k + \frac{\xi_i^k}{r} \right) \mathrm{dx}}{\int_\Omega \left(b_1^k\right)^2 \mathrm{dx}}. \tag{23}$$

- *The subproblems* (21c) *and* (21d). These subproblems can be rewritten as

$$\begin{aligned} \min_{b_1} \ \alpha \int_\Omega |\nabla b_1|^2 \mathrm{dx} + \frac{r}{2} \int_\Omega \left(p_1^k - \left(I - b_1 c_1^{k+1} - b_2^k\right) - \frac{\xi_1^k}{r} \right)^2 \mathrm{dx} \\ + \nu \int_\Omega (b_1 - 1)^2 \mathrm{dx} + \frac{r}{2} \int_\Omega \left(p_2^k - \left(I - b_1 c_2^{k+1} - b_2^k\right) - \frac{\xi_2^k}{r} \right)^2 \mathrm{dx}, \end{aligned}$$

where ν is a constant parameter. This problem is smooth and convex and then the optimization condition can be written as

$$\left(-2\alpha\Delta + \left(2\nu + r\left(c_1^{k+1}\right)^2 + r\left(c_2^{k+1}\right)^2 \right) \mathcal{I} \right) b_1^{k+1} = r c_1^{k+1} \left(I - p_1^k - b_2^k + \frac{\xi_1^k}{r} \right) + r c_2^{k+1} \left(I - p_2^k - b_2^k + \frac{\xi_2^k}{r} \right) + 2\nu\mathcal{I},$$

where $\mathcal{I}$ is the identity operator. This equation is the linear equation, which numerical method depends on the structure of the left matrix operator. This matrix is positive definite and then the conjugate gradient method can be used to solve it. However, we here assume that the discretization of the gradient operator in the numerical implementations uses the periodic boundary condition, so the fast Fourier transform can be solved efficiently. More specifically, the solution of the equation of this equation can be obtained by

$$b_1^{k+1} = \mathcal{F}^{-1} \left(\frac{r c_1^{k+1} \mathcal{F}\left(I - p_1^k - b_2^k + \frac{\xi_1^k}{r} \right) + r c_2^{k+1} \mathcal{F}\left(I - p_2^k - b_2^k + \frac{\xi_2^k}{r} \right) + 2\nu\mathcal{F}(\mathcal{I})}{\left(2\nu + r(c_1^{k+1})^2 + r(c_2^{k+1})^2 \right) \mathcal{F}(\mathcal{I}) - 2\alpha\mathcal{F}(\Delta)} \right), \tag{24}$$

where $\mathcal{F}$ is the Fourier transform and $\mathcal{F}^{-1}$ denotes as inverse Fourier transform.

Similarly, the solution of the problem (21c) can be got by

$$b_2^{k+1} = \mathcal{F}^{-1} \left(\frac{r\mathcal{F}\left(I - p_1^k - b_1^{k+1} c_1^{k+1} + \frac{\xi_1^k}{r} \right) + r\mathcal{F}\left(I - p_2^k - b_1^{k+1} c_2^{k+1} + \frac{\xi_2^k}{r} \right)}{2r\mathcal{F}(\mathcal{I}) - 2\beta\mathcal{F}(\Delta)} \right). \tag{25}$$

- *The subproblems* (21e) *and* (21f). The optimization problem with respect to variable $p_i, i = 1, 2.$ is expressed as

$$\begin{cases} p_1^{k+1} & = \operatorname*{argmin}_{p_1} \lambda \int_\Omega p_1^2 u^k \mathrm{dx} + \frac{r}{2} \int_\Omega \left(p_1 - \left(I - b_1^{k+1} c_1^{k+1} - b_2^{k+1}\right) - \frac{\xi_1^k}{r} \right)^2 \mathrm{dx}, \\ p_2^{k+1} & = \operatorname*{argmin}_{p_2} \lambda \int_\Omega p_2^2 \left(1 - u^k\right) \mathrm{dx} + \frac{r}{2} \int_\Omega \left(p_2 - \left(I - b_1^{k+1} c_2^{k+1} - b_2^{k+1}\right) - \frac{\xi_2^k}{r} \right)^2 \mathrm{dx}. \end{cases}$$

This optimization problem is smooth and then the solution can be obtained by

$$\begin{cases} p_1^{k+1} & = \frac{r\left(I - b_1^{k+1} c_1^{k+1} - b_2^{k+1}\right) + \xi_1^k}{2\lambda u^k + r}, \\ p_2^{k+1} & = \frac{r\left(I - b_1^{k+1} c_2^{k+1} - b_2^{k+1}\right) + \xi_2^k}{2\lambda\left(1 - u^k\right) + r}. \end{cases} \tag{26}$$

3.2.2. The subproblem (19b)

Now we consider to solve the non-smooth and convex subproblem (19b). The main challenge is how efficiently to overcome the non-smooth of the proposed numerical method. To this end, we employ the ADMM by breaking the problem (19b) into smaller problems and hence making them easier to be handled [4, 43, 45]. That is to say, by introducing the auxiliary variable $\mathbf{q} = \nabla u$, the corresponding optimization problem can be written as

$$\begin{cases} \min\limits_{u} & \lambda \int_\Omega \mathcal{S} u \mathrm{dx} + \int_\Omega |\mathbf{q}| \mathrm{dx} + \Gamma_{\mathcal{D}}(u), \\ \text{s.t.} & \mathbf{q} = \nabla u. \end{cases} \tag{27}$$

With the help of the augmented Lagrangian method, we have the following saddle point problem

$$\min_{u,\mathbf{q}} \max_{\boldsymbol{\xi}_3} \mathcal{L}_\tau(u, \mathbf{q}; \boldsymbol{\xi}_3) = \lambda \int_\Omega \mathcal{S} u \mathrm{dx} + \int_\Omega |\mathbf{q}| \mathrm{dx} - \int_\Omega \boldsymbol{\xi}_3^T (\mathbf{q} - \nabla u) \mathrm{dx} + \frac{\tau}{2} \int_\Omega (\mathbf{q} - \nabla u)^2 \mathrm{dx} + \Gamma_{\mathcal{D}}(u),$$

where $\boldsymbol{\xi}_3$ is the Lagrange multiplier, τ represents the penalty parameter. Under the framework of the ADMM, we can alternatively solve the optimization variable u^{k+1}, the auxiliary variable $\mathbf{q}^{k+1}$ and the Lagrangian multiplier $\boldsymbol{\xi}_3^{k+1}$ as follows

$$\begin{cases} u^{k+1} = \operatorname*{argmin}_{u} \ \mathcal{L}_\tau(u, \mathbf{q}^k; \boldsymbol{\xi}_3^k), & \text{(28a)} \\ \mathbf{q}^{k+1} = \operatorname*{argmin}_{\mathbf{q}} \ \mathcal{L}_\tau(u^{k+1}, \mathbf{q}; \boldsymbol{\xi}_3^k), & \text{(28b)} \\ \boldsymbol{\xi}_3^{k+1} = \boldsymbol{\xi}_3^k - \tau(\mathbf{q}^{k+1} - \nabla u^{k+1}). & \text{(28c)} \end{cases}$$

In the following, we consider the details to solve the subproblems (28a)-(28b)

- To the subproblem (28a), it can be rewritten as

$$u^{k+1} = \operatorname*{argmin}_{u \in [0,1]} \lambda \int_\Omega \mathcal{S} u \mathrm{dx} - \int_\Omega \boldsymbol{\xi}_3^k (\mathbf{q}^k - \nabla u) \mathrm{dx} + \frac{\tau}{2} \int_\Omega (\mathbf{q}^k - \nabla u)^2 \mathrm{dx} + \Gamma_{\mathcal{D}}(u), \tag{29}$$

which is convex and smooth. Then the optimal solution u^{k+1} satisfy the following optimal equation

$$\tau \Delta u^{k+1} = \lambda \mathcal{S} + \tau \mathrm{div} \left(\mathbf{q}^k - \frac{\boldsymbol{\xi}_3^k}{\tau} \right) + \partial \Gamma_{\mathcal{D}}(u), \ u^{k+1} \in [0, 1]. \tag{30}$$

To above linear equation, we solve it by using the Gauss-Seidel method with centered and backward differences for Laplace and divergence operators. Thus, we have

$$u_{i,j}^{k+1} = \frac{1}{4} \left[\left(u_{i+1,j}^{k+1} + u_{i-1,j}^{k+1} + u_{i,j+1}^{k+1} + u_{i,j-1}^{k+1} \right) - \frac{\lambda \mathcal{S}}{\tau} + \zeta_{i,j} \right],$$

where

$$\zeta_{i,j} = \mathbf{q}_{i,j}^k + \mathbf{q}_{i-1,j}^k + \mathbf{q}_{i,j}^k + \mathbf{q}_{i,j-1}^k - \frac{1}{\tau} \left([\boldsymbol{\xi}_3^k]_{i,j} + [\boldsymbol{\xi}_3^k]_{i-1,j} + \left[\boldsymbol{\xi}_3^k\right]_{i,j} + \left[\boldsymbol{\xi}_3^k\right]_{i,j-1} \right).$$

Taking the constraint by projecting u^{k+1} into $[0, 1]$, we have

$$u_{i,j}^{k+1} = \min \left\{ \max \left\{ u_{i,j}^{k+1}, 0 \right\}, 1 \right\}. \tag{31}$$

- To the subproblem (28b), we can rewritten as

$$\mathbf{q}^{k+1} = \operatorname*{argmin}_{\mathbf{q}} \int_\Omega |\mathbf{q}| \mathrm{dx} - \int_\Omega \left(\boldsymbol{\xi}_3^k \right)^T (\mathbf{q} - \nabla u^{k+1}) \mathrm{dx} + \frac{\tau}{2} \int_\Omega (\mathbf{q} - \nabla u^{k+1})^2 \mathrm{dx}.$$

This problem is the classical $L^1 - L^2$ problem and then we can get the closed-form solution as

$$\mathbf{q}^{k+1} = \mathrm{shrinkage} \left(\nabla u^{k+1} + \frac{\boldsymbol{\xi}_3^k}{\tau}, \frac{1}{\tau} \right). \tag{32}$$

Algorithm 1 The algorithm of the hybrid bias field correction image segmentation model (8).

Input: Input image I, parameters λ, penalty parameters r, τ, ν, bias parameters α, β, maximum iteration K_{max} and stopping threshold ϵ.
Initialize: Setting the initial values $u^0 = b_2^0 = p_i^0 = c_i^0 = \mathbf{q}^0 = \mathbf{0}, i = 1, 2.$ $b_1^0 = \mathcal{I}$, the parameters $\lambda, \alpha, \beta > 0$, let $k = 1$ and start k-th iteration. Let $k = k + 1$ return to the $k + 1$ iteration till converge.
while (not converged and $k \leq K_{\max}$) **do**
  Compute $c_i^{k+1}, i = 1, 2.$ from Eq.(23) by fixing other variables;
  Compute $b_i^{k+1}, i = 1, 2.$ from Eq.(24) and Eq.(25) by fixing other variables;
  Compute $p_i^{k+1}, i = 1, 2.$ from Eq.(26) by fixing other variables;
  Update ξ_1^{k+1}, ξ_2^{k+1} from Eq.(28c) and Eq.(21g);
  Compute $\mathcal{S}^{k+1}$ by $\mathcal{S}^{k+1} = (I - b_1^{k+1}c_1^{k+1} - b_2^{k+1})^2 - (I - b_1^{k+1}c_2^{k+1} - b_2^{k+1})^2$;
  while $(\|u^{k+1} - u^k\|_1/\|u^k\|_1 \leq \epsilon)$ **do**
    Compute u^{k+1} from Eq. (31) by fixing other variables;
    Compute $\mathbf{q}^{k+1}$ from Eq. (32) by fixing other variables;
    Update $\boldsymbol{\xi}_3^{k+1}$ from Eq. (21h);
  end while
end while
output: Segmentation result $u = u^{k+1}$.

More specifically, the algorithm to solve the model (8) is summarized as follows.

Remark 3.3. *To Algorithm 1, it includes two inner iterations as* (21a)-(21h) *and* (28a)-(28c)*. To the iteration* (21a)-(21h)*, it is used to solve the nonconvex optimization problem* (19a)*. We do not expect to get the optimization. However, the iteration* (28a)-(28c) *is of using the ADMM [3, 10] to solve the convex optimization problem. So the convergence can be kept.*

3.3. Partial Convergence Analysis

The convergence of ADMM for non-convex composite problems has been proved in reference [44]. Here, we discuss the partial convergence analysis of Algorithm 1 for image segmentation problem.

Theorem 3.2. *Assume that* $u^{k+1} - u^k \to 0$*,* $\xi_1^{k+1} - \xi_1^k \to 0$*,* $\xi_2^{k+1} - \xi_2^k \to 0$ *and* $\boldsymbol{\xi}_3^{k+1} - \boldsymbol{\xi}_3^k \to 0$ *as* $k \to \infty$ *in Algorithm 1, the sequence* $\{A^k = (c_i^k, b_i^k, p_i^k, u^k, \mathbf{q}^k, \xi_1^k, \xi_2^k, \boldsymbol{\xi}_3^k)\}_{(i=1,2)}$ *generated by the Algorithm 1 converges to a limit point* $A^* = (c_i^*, b_i^*, p_i^*, u^*, \mathbf{q}^*, \xi_1^*, \xi_2^*, \boldsymbol{\xi}_3^*)_{(i=1,2)}$*, then this limit point* A^* *is a Karush-Kuhn-Tucker (KKT) point of problem* (20) *and* (27)*, i.e.,*

$$\left\{\begin{array}{l} \int_\Omega b_1^* \xi_i^* \mathrm{dx} = 0, \\ \sum_{i=1}^2 c_i^* \xi_i^* + 2\nu\mathcal{I} + 2(\alpha\Delta - \nu)b_1^* = 0, \\ \sum_{i=1}^2 \xi_i^* + 2\beta\Delta b_2^* = 0, \\ \xi_1^* - 2\lambda u^* p_1^* = 0, \\ \xi_2^* - 2\lambda(1 - u^*)p_2^* = 0. \end{array}\right. \quad \text{and} \quad \left\{\begin{array}{l} \lambda[(p_1^*)^2 - (p_2^*)^2] - \mathrm{div}\boldsymbol{\xi}_3^* + \partial\Gamma_{\mathcal{D}}(u) = 0, \\ p_i^* = I - b_1^* c_i^* - b_2^*, \\ \partial|\mathbf{q}^*| - \boldsymbol{\xi}_3^* = 0, \\ \mathbf{q}^* = \nabla u^*. \end{array}\right. \tag{33}$$

for $i = 1, 2$.

Proof. The proof uses the same ideas as one of Theorems in [13], which is given in the appendix. □

4. Experimental

4.1. Experiment Introduction

To verify the feasibility and effectiveness of our proposed model, we conduct experiments to segment both natural images and medical images. The medical images contain two different datasets, one is a publicly available online brain glioma dataset and the other is a real MRI lesion segmentation dataset from a hospital. Throughout this section, we also conduct comparative experiments with several models such as ICTM [39], CVE [49], WBHMS [45], LIC [16], L1PS [13], AWCA[30], DEMCV [47]. We denote our model by OURS. In this paper, we discuss the experimental results and segmentation metrics of our proposed method and the comparison method, as well as the running time. All inputting images are rescaled to be in the range [0,1]. Figure 2–4 show the segmentation results and analysis of nature images. Figure 5 is the energy function diagram. Figure 6–7 show the medical image segmentation results. Table 1–4 show the index values of the natural image and medical image segmentation results. All experiments are performed using MATLAB(R2021a) on a windows(10)(64bit) desktop computer with an Intel Core i7 3.20 GHz processor and 16.0GB of RAM.

4.2. Parameter Rules

Here we discuss the choices of the parameters used in our proposed model and the models of the comparative experiment. Throughout all experiments, we set the maximum number of iterations as $K_{\max} = 300$ and the termination condition error is $\epsilon = 10^{-4}$. The variables involved in our method are the data fidelity parameter λ, the weights α and β of the bias field, the weight parameter ν, and the penalty parameters r and τ.

There are many parameters used in the proposed model. The main adjustment parameters are λ, α and β. Then, fine-tune the other parameters. Due to the differences between natural images and medical images, the ranges of parameters are different. So, we next discuss the parameter selection ranges separately. By the trial-and-error method to obtain ideal results, for natural images, here we fix the parameter $r = 1$ and set the range of λ, α and β are $\lambda \in [10, 70]$, $\alpha \in [10^2, 10^4]$, $\beta \in [10^2, 10^4]$, the range of other parameters are $\tau \in [1, 10]$ and $\nu \in [0.01, 10]$, respectively. Firstly, we adjust the parameter the data fidelity parameter λ, then adjust the parameter weights α and β of the bias fields, and finally adjust the penalty parameters ν and τ. We note that the magnitude of the smooth term parameters is strongly correlated with the strength of the grayscale inhomogeneity in a given image. Then, we discuss the influence of the smooth parameters α and β on the segmentation results in Figure 4. For glioma images, we fix the parameters $r = 0.05$, $\tau = 0.02$ and $\nu = 0.1$, the range of other parameters are $\lambda \in [20, 49]$, $\alpha \in [50, 300]$ and $\beta \in [100, 400]$, respectively. For the real MRI lesion dataset, getting accurate segmentation is very challenging due to the very low contrast of the images and the blurred boundaries of the lesion areas. Therefore, the selection range of parameters is different from the previous data. We set $\lambda \in [10, 80]$, $\alpha \in [10^3, 10^4]$ and $\beta \in [5 \times 10^3, 10^4]$, the other parameters are $r \in [0.1, 2]$, $\tau \in [0.001, 0.1]$ and $\nu \in [0.1, 2]$.

Next, we consider the range of parameters involved in the comparative models. We refer to the corresponding literature and then adjust the parameters to obtain ideal results. The related details are summarized as follows.

1) WBHMS [45]: The WBHMS model is a weighted bounded hessian variational model. Here we set the data fidelity parameter $\lambda \in [0.4, 20]$, the penalty parameters $r_1 \in [0.3, 20]$, $r_2 \in [0.1, 8]$ and $r_3 \in [0.005, 2]$, the value ranges of piecewise constants $c_1 \in [0.01, 0.45]$ and $c_2 \in [0.51, 0.90]$.
2) ICTM [39]: The ICTM model is an efficient iterative thresholding method, the parameters are the data fidelity parameter $\lambda \in [0.02, 0.083]$ and the time step $\delta \in [0, 0.1]$.
3) LIC [16]: The LIC model is a local intensity clustering model. Here we set the data fidelity parameter $\lambda = 1$, the length parameter $\nu = 0.001 * 255 * 255$, the Gaussian kernel parameter $\sigma \in [15, 40]$, the level set regularization parameter $\mu = 1$, the constant parameter in the Heaviside-Dirac function $\varepsilon = 1$ and the time step $\delta = 0.1$.
4) L1PS [13]: To the L1PS model, the data fidelity term parameter $\lambda \in [1, 10^3]$, the length term parameter $\nu = 1$, the smooth term parameter $\alpha \in \{2.5 * 10^5, 5 * 10^5\}$, the penalty parameters $r_1 = \{10, 50\}$ and $r_2 = \lambda$.
5) CVE [49]: The CVE model is an Eulers elastica model based on Chan-Vese's segmentation model. The parameters $a = 0.001$, $b \in [0.5, 6]$, the regularization parameter $\eta \in [0.5, 6]$, the penalty parameters $r_1 = 1$, $r_2 \in [0.5, 6]$, $r_3 \in [0.1, 0.5]$ and $r_4 \in [0.8, 2]$.
6) AWCA [30]: The AWCA model is an adaptive weighted curvature-based active contour model. The parameters $\lambda \in [130, 140]$, $r \in [1, 2]$, $\tau \in [0.002, 0.006]$.
7) DEMCV [47]: The DEMCV model is a dual expectation-maximization (EM) algorithm for total variation (TV) regularized Gaussian mixture model. The smooth parameter $\delta \in [1, 1000]$, the regularization parameter $\gamma \in [10, 40]$.

4.3. Evaluation Indicators

In the numerical experiment part, we use four metrics, namely Jaccard Similarity, Accuracy, F1-Score, κ-coefficient [45] to objectively evaluate the segmentation results. The closer the values of these indicators are to 1, the closer the experimental results are to the ground truth. Next, we discuss the influence of different images and parameters in the experiments on the results.

1) Jaccard Similarity (JS) coefficient is used to measure the similarity and difference between the segmentation result S_1 and the ground truth S_2. JS is defined as:

$$\mathrm{JS} = \frac{|S_1 \cap S_2|}{|S_1 \cup S_2|}.$$

where $|\cdot|$ represents the number of pixels in the image area.

2) Pixel accuracy is a common evaluation index to evaluate the segmentation result. It is used to calculate the percentage of pixels correctly classified in the segmentation results of the model. Accuracy is defined as:

$$\mathrm{Accuracy} = \frac{\mathrm{TP}+\mathrm{TN}}{\mathrm{TP}+\mathrm{TN}+\mathrm{FP}+\mathrm{FN}}.$$

where TP represents the number of real samples, TN represents the number of true negative samples, FP represents the number of false positive samples, FN represents the number of false negative samples.

3) In the two-phase segmentation problem, F1-score is a measure of the accuracy of segmentation results. This measure integrates the accuracy and recall of model segmentation results, and is a harmonic average of these two evaluation indexes. F1-score (F1) is defined as:

$$\mathrm{F1} = \frac{2 * \mathrm{PR}}{\mathrm{P}+\mathrm{R}}, \text{ with } \mathrm{P} = \frac{\mathrm{TP}}{\mathrm{TP}+\mathrm{FP}}, \ \mathrm{R} = \frac{\mathrm{TP}}{\mathrm{TP}+\mathrm{FN}}.$$

4) κ-coefficient is an index to measure classification accuracy based on confusion matrix and is defined as

$$\kappa = \frac{\mathrm{ACC}-\mathrm{P_c}}{1-\mathrm{P_c}}, \text{ with } \mathrm{P_c} = \frac{(\mathrm{TP}+\mathrm{FN})(\mathrm{TP}+\mathrm{FP})+(\mathrm{FP}+\mathrm{TN})(\mathrm{FN}+\mathrm{TN})}{(\mathrm{TP}+\mathrm{TN}+\mathrm{FP}+\mathrm{FN})^2}.$$

4.4. Natural Images

Here we evaluate our proposed method quantitatively and compare it with the after-mentioned models, where the testing images as shown in Figure 2. These datasets are downloaded from the website [1], and we number the selected images and select the same initial contours for experiments. The quantitative results by using the chosen indicators are shown in Table 1. It is obvious that our method is superior not only in the mean but also in the standard deviation compared with other models. These imply the robustness and the stability of our proposed model.

In image segmentation models, it is well known that the accuracy and the effectiveness also depend on the selection of initial contour. To this end, we randomly choose two testing images from Figure 2 to compare these effects for different models. From left to right, they are #11-c_1, #11-c_2, #11-c_3, #12-c_1, #12-c_2 and #12-c_3. From top to bottom, the initial contours and the experimental results of each method are shown in order. To fairness, we choose three original contours to be outside, intersecting and inside the segmentation target. The relevant evaluation indicators are listed in Table 2. It is easy to observe that our proposed model outperforms other models in most cases from these indexes. Especially, Our proposed model has optimal mean and standard deviation, these imply the robustness and stability of our proposed model. From a visual point of view, our proposed model can efficiently segment image details such as the wings and tail of the 'fish' and the target on the board as shown in Figure 3.

In our proposed model, the smoothing of the bias fields b_1 and b_2 depends on the choice of the parameters α and β. We note that the magnitude of the smooth term parameters are strongly correlated with the strength of the gray scale inhomogeneity in a given image. Here we consider the effect of parameters by choosing Figure 2#3 as the testing image. From the plot of the evaluation indexes, we choose the range of the parameters are $(\alpha,\beta) \in [40,800]\times[40,800]$ to observe the influence of the parameters α and β. It is obvious that both α and β affect the segmentation results. As

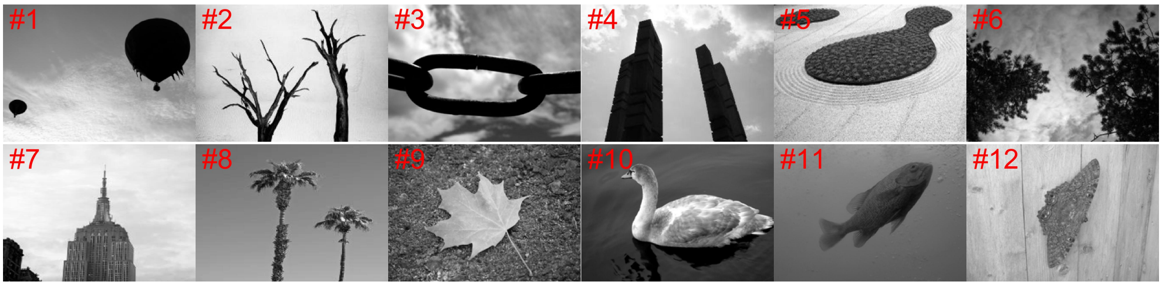

Figure 2. Evaluation and comparison on natural images downloaded from the Weizmann segmentation datasets.

Criterions	JS								Accuracy							
Images	WBHMS	ICTM	LIC	L1PS	CVE	AWCA	DEMCV	OURS	WBHMS	ICTM	LIC	L1PS	CVE	AWCA	DEMCV	OURS
#1	0.9545	0.9538	0.9829	0.9818	0.9814	0.9839	0.9837	0.9831	0.9938	0.9937	0.9978	0.9976	0.9976	0.9979	0.9979	0.9978
#2	0.8398	0.8356	0.8522	0.8450	0.8602	0.8381	0.8368	0.8612	0.9778	0.9773	0.9795	0.9785	0.9798	0.9776	0.9774	0.9806
#3	0.9131	0.6844	0.9089	0.8803	0.8888	0.9160	0.7314	0.9185	0.9782	0.8935	0.9771	0.9690	0.9723	0.9791	0.9149	0.9797
#4	0.9929	0.9936	0.9945	0.9946	0.9902	0.9943	0.9824	0.9946	0.9980	0.9982	0.9984	0.9985	0.9972	0.9984	0.9950	0.9985
#5	0.9718	0.9735	0.9686	0.9734	0.9690	0.9704	0.9680	0.9751	0.9922	0.9927	0.9913	0.9927	0.9914	0.9919	0.9912	0.9931
#6	0.9098	0.9157	0.9125	0.9244	0.9132	0.9104	0.7821	0.9304	0.9556	0.9585	0.9572	0.9628	0.9563	0.9561	0.8924	0.9659
#7	0.9645	0.9643	0.9667	0.9675	0.9799	0.9914	0.9787	0.9717	0.9931	0.9930	0.9935	0.9936	0.9961	0.9931	0.9958	0.9945
#8	0.7541	0.6907	0.7720	0.7443	0.7417	0.7122	0.4764	0.8737	0.9696	0.9617	0.9717	0.9683	0.9671	0.9643	0.8681	0.9839
#9	0.9254	0.7776	0.8985	0.9251	0.9153	0.9085	0.9799	0.9574	0.9865	0.9515	0.9819	0.9866	0.9846	0.9834	0.9832	0.9924
#10	0.8867	0.7110	0.4094	0.9073	0.8821	0.6400	0.9025	0.9433	0.9723	0.9298	0.7132	0.9775	0.9711	0.9126	0.9182	0.9862
Mean	0.9113	0.8500	0.8666	0.9132	0.9122	0.8865	0.8622	**0.9409**	0.9817	0.9650	0.9562	0.9825	0.9814	0.9754	0.9534	**0.9873**
Std	0.0676	0.1190	0.1654	0.0762	0.0721	0.1160	0.1557	**0.0431**	0.0127	0.0097	0.0819	0.0124	0.0137	0.0248	0.0470	**0.0096**
Criterions	F1-score								κ							
Images	WBHMS	ICTM	LIC	L1PS	CVE	AWCA	DEMCV	OURS	WBHMS	ICTM	LIC	L1PS	CVE	AWCA	DEMCV	OURS
#1	0.9767	0.9764	0.9914	0.9908	0.9906	0.9919	0.9918	0.9915	0.9732	0.9727	0.9901	0.9895	0.9892	0.9907	0.9905	0.9902
#2	0.9129	0.9104	0.9202	0.9160	0.9248	0.9119	0.9111	0.9254	0.9003	0.8975	0.9085	0.9037	0.9132	0.8992	0.8983	0.9143
#3	0.9546	0.8126	0.9523	0.9363	0.9411	0.9562	0.8449	0.9575	0.9402	0.7399	0.9372	0.9159	0.9231	0.9424	0.7870	0.9442
#4	0.9964	0.9968	0.9973	0.9973	0.9951	0.9972	0.9911	0.9973	0.9950	0.9955	0.9962	0.9962	0.9931	0.9960	0.9871	0.9962
#5	0.9857	0.9866	0.9840	0.9865	0.9843	0.9850	0.9838	0.9875	0.9803	0.9815	0.9781	0.9815	0.9784	0.9794	0.9777	0.9828
#6	0.9528	0.9560	0.9542	0.9607	0.9546	0.9531	0.8777	0.9639	0.9110	0.9169	0.9141	0.9255	0.9124	0.9120	0.7834	0.9316
#7	0.9820	0.9518	0.9831	0.9835	0.9899	0.9957	0.9892	0.9857	0.9777	0.9775	0.9791	0.9795	0.9874	0.9776	0.9866	0.9822
#8	0.8598	0.8171	0.8713	0.8534	0.8517	0.8319	0.6453	0.9326	0.8431	0.7965	0.8557	0.8360	0.8334	0.8125	0.5754	0.9235
#9	0.9613	0.8749	0.9466	0.9611	0.9558	0.9520	0.9898	0.9782	0.9531	0.8451	0.9357	0.9530	0.9465	0.9420	0.9412	0.9736
#10	0.9399	0.8311	0.5810	0.9514	0.9373	0.7805	0.9488	0.9708	0.9220	0.7884	0.3898	0.9368	0.9187	0.7292	0.7490	0.9618
Mean	0.9522	0.9114	0.9181	0.9537	0.9525	0.9355	0.9174	**0.9690**	0.9396	0.8912	0.8885	0.9418	0.9395	0.9181	0.8676	**0.9600**
Std	0.0386	0.0687	0.1180	0.0414	0.0412	0.0703	0.1038	**0.0232**	0.0441	0.0885	0.1713	0.0469	0.0475	0.0819	0.1323	**0.0281**

Table 1. The index values of the segmentation results of our model and the comparison models in natural images.

Criterions	JS								Accuracy							
Images	WBHMS	ICTM	LIC	L1PS	CVE	AWCA	DEMCV	OURS	WBHMS	ICTM	LIC	L1PS	CVE	AWCA	DEMCV	OURS
#11-c_1	0.8110	0.7723	0.8633	0.8979	0.8465	0.7730	0.2940	0.9103	0.9670	0.9602	0.9761	0.9821	0.9729	0.9603	0.5830	0.9843
#11-c_2	0.8095	0.7880	0.8652	0.9028	0.8326	0.7707	0.2948	0.9095	0.9667	0.9629	0.9764	0.9830	0.9707	0.9599	0.5863	0.9841
#11-c_3	0.8112	0.7593	0.8669	0.9192	0.8407	0.7694	0.2937	0.9078	0.9670	0.9579	0.9767	0.9859	0.9721	0.9597	0.5821	0.9839
#12-c_1	0.9438	0.9314	0.9531	0.9497	0.9583	0.9381	0.8610	0.9734	0.9924	0.9906	0.9936	0.9909	0.9944	0.9914	0.9790	0.9964
#12-c_2	0.9278	0.9314	0.9694	0.9672	0.9575	0.9404	0.8712	0.9512	0.9902	0.9906	0.9959	0.9956	0.9942	0.9917	0.9806	0.9934
#12-c_3	0.9251	0.9294	0.9650	0.9519	0.9575	0.9424	0.8690	0.9479	0.9899	0.9903	0.9953	0.9934	0.9947	0.9920	0.9803	0.9930
Mean	0.8714	0.8520	0.9138	0.9315	0.8989	0.8557	0.5806	**0.9334**	0.9789	0.9754	0.9857	0.9885	0.9832	0.9758	0.7819	**0.9892**
Std	0.0611	0.0792	0.0489	0.0262	0.0591	0.0846	0.2865	**0.0255**	0.0120	0.0152	0.0093	0.0051	0.0113	0.0159	0.1981	**0.0052**
Criterions	F1-score								κ							
Images	WBHMS	ICTM	LIC	L1PS	CVE	AWCA	DEMCV	OURS	WBHMS	ICTM	LIC	L1PS	CVE	AWCA	DEMCV	OURS
#11-c_1	0.8957	0.8715	0.9266	0.9462	0.9168	0.8720	0.4543	0.9530	0.8763	0.8484	0.9124	0.9356	0.9008	0.8489	0.2530	0.9436
#11-c_2	0.8947	0.8814	0.9277	0.9489	0.9086	0.8705	0.4554	0.9526	0.8752	0.8598	0.9138	0.9387	0.8914	0.8473	0.2548	0.9431
#11-c_3	0.8958	0.8632	0.9287	0.9579	0.9135	0.8697	0.4540	0.9517	0.8761	0.8389	0.9149	0.9494	0.8970	0.8463	0.2523	0.9420
#12-c_1	0.9711	0.9634	0.9760	0.9806	0.9754	0.9681	0.9248	0.9865	0.9667	0.9578	0.9723	0.9803	0.9787	0.9631	0.9126	0.9845
#12-c_2	0.9625	0.9634	0.9845	0.9808	0.9783	0.9693	0.9311	0.9750	0.9569	0.9578	0.9821	0.9769	0.9750	0.9645	0.9199	0.9712
#12-c_3	0.9611	0.9634	0.9822	0.9753	0.9789	0.9704	0.9299	0.9732	0.9553	0.9578	0.9795	0.9715	0.9750	0.9657	0.9185	0.9692
Mean	0.9302	0.9177	0.9543	0.9650	0.9453	0.9200	0.6916	**0.9653**	0.9178	0.9034	0.9458	0.9587	0.9363	0.9060	0.5852	**0.9589**
Std	0.0349	0.0460	0.0267	0.0145	0.0324	0.0493	0.2370	**0.0136**	0.0420	0.0547	0.0323	0.0182	0.0400	0.0585	0.3318	**0.0167**

Table 2. The index values of the segmentation results of our model and the comparison models for different initial contours.

the parameters α and β become larger, the segmentation index also increases. When the gray level inhomogeneity of the image is relatively large, we choose a large value of β, and then adjust the parameter α.

To check the convergence of the proposed algorithm, we plot the curve of the energy functional $E(u, b_1, b_2, c_1, c_2)$ defined in (8) against the iteration for segmenting two testing images #4 and #7 in Figure 2. It is easy to observe that $E(u, b_1, b_2, c_1, c_2)$ shows a decreasing trend based on Figure 5 and then this fact implies the convergence of the proposed algorithm.

[1]https://www.wisdom.weizmann.ac.il/∼vision.

Figure 3. Segmentation results of our and comparative models in natural images #11,#12 are shown.

4.5. *Medical Images*

Medical image segmentation aims to make anatomical or pathological structures changes in more clear in images, it often plays a key role in computer-aided diagnosis and smart medicine due to the great improvement in diagnostic efficiency and accuracy. However, the intensity inhomogeneity and noises often occur in real medical images, which present a large degree of challenge to image segmentation.

Glioma in humans has a great impact on the health of the human body [26]. It is difficult to segment Glioma and its internal structure because the Glioma boundaries have edemas and complex internal structures. To compare the

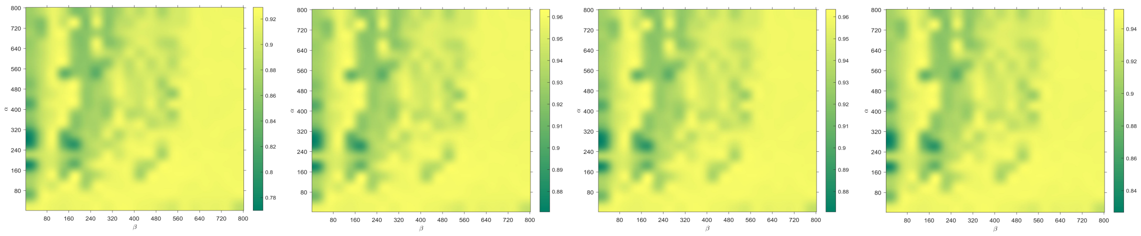

(a) JS (b) Accuracy (c) F1-Score (d) κ

Figure 4. The influence of parameters α and β on the segmentation results in image #3, where $(\alpha, \beta) \in [40, 800] \times [40, 800]$.

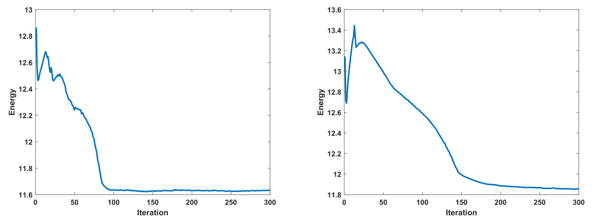

Figure 5. The numerical energy of images #4 and #7.

Criterions	JS								Accuracy							
Images	WBHMS	ICTM	LIC	L1PS	CVE	AWCA	DEMCV	OURS	WBHMS	ICTM	LIC	L1PS	CVE	AWCA	DEMCV	OURS
T1-c_1	0.2053	0.2053	0.2226	0.1653	0.5804	0.8373	0.2076	0.8990	0.9337	0.9243	0.9267	0.8973	0.9901	0.9960	0.9229	0.9978
T1-c_2	0.2065	0.2047	0.2011	0.1819	0.5808	0.2307	0.2075	0.8942	0.9220	0.9251	0.9167	0.9165	0.9902	0.9381	0.9228	0.9975
T1-c_3	0.2034	0.2036	0.2008	0.1880	0.5808	0.2216	0.2076	0.8980	0.9301	0.9251	0.9167	0.9100	0.9902	0.9359	0.9229	0.9977
Mean	0.2051	0.2045	0.2082	0.1784	0.5807	0.4299	0.2076	**0.8971**	0.9286	0.9248	0.9200	0.9079	0.9902	0.9567	0.9929	**0.9977**
Std	0.0013	0.0007	0.0102	0.0096	0.0002	0.2881	0.0000	**0.0021**	0.0049	0.0004	0.0047	0.0080	0.0000	0.0278	0.0000	**0.0001**
T2-c_1	0.3827	0.3812	0.3049	0.3325	0.8011	0.4158	0.3793	0.9244	0.9638	0.9536	0.9346	0.9444	0.9933	0.9619	0.9526	0.9977
T2-c_2	0.4272	0.3813	0.3135	0.3368	0.8307	0.4158	0.3790	0.9243	0.9683	0.9536	0.9366	0.9443	0.9943	0.9640	0.9525	0.9977
T2-c_3	0.4401	0.3813	0.3234	0.3624	0.8316	0.3543	0.3778	0.9198	0.9664	0.9530	0.9398	0.9491	0.9943	0.9645	0.9523	0.9975
Mean	0.4167	0.3813	0.3139	0.3439	0.8211	0.3953	0.3787	**0.9228**	0.9662	0.9534	0.9370	0.9459	0.9940	0.9635	0.9525	**0.9976**
Std	0.0246	0.0000	0.0076	0.0132	0.0142	0.0290	0.0006	**0.0021**	0.0018	0.0003	0.0021	0.0022	0.0005	0.0011	0.0001	**0.0001**
Criterions	F1-score								κ							
Images	WBHMS	ICTM	LIC	L1PS	CVE	AWCA	DEMCV	OURS	WBHMS	ICTM	LIC	L1PS	CVE	AWCA	DEMCV	OURS
T1-c_1	0.3407	0.3406	0.3642	0.2838	0.7345	0.9114	0.3439	0.9468	0.3180	0.3171	0.3415	0.2570	0.7296	0.9040	0.3203	0.9457
T1-c_2	0.3423	0.3398	0.3348	0.3075	0.7348	0.3749	0.3437	0.9442	0.3187	0.3163	0.3106	0.2825	0.7299	0.3534	0.3201	0.9429
T1-c_3	0.3381	0.3383	0.3344	0.3165	0.7348	0.3628	0.3439	0.9463	0.3149	0.3148	0.3102	0.2914	0.7299	0.3408	0.3203	0.9451
Mean	0.3404	0.3396	0.3445	0.3026	0.7347	0.5497	0.3438	**0.9458**	0.3172	0.3161	0.3208	0.2770	0.7298	0.5327	0.3202	**0.9446**
Std	0.0017	0.0010	0.0140	0.0138	0.0001	0.2558	0.0001	**0.0011**	0.0017	0.0010	0.0147	0.0146	0.0001	0.2626	0.0001	**0.0012**
T2-c_1	0.5536	0.5520	0.4673	0.4991	0.8896	0.5874	0.5500	0.9607	0.5378	0.5323	0.4424	0.4765	0.8861	0.5702	0.5300	0.9595
T2-c_2	0.5986	0.5521	0.4773	0.5039	0.9075	0.5873	0.5496	0.9607	0.5832	0.5324	0.4773	0.4814	0.9046	0.5698	0.5297	0.9595
T2-c_3	0.5721	0.5498	0.4887	0.5320	0.9081	0.5232	0.5484	0.9582	0.5558	0.5299	0.4887	0.5110	0.9051	0.5016	0.5284	0.9570
Mean	0.5748	0.5513	0.4778	0.5117	0.9017	0.5660	0.5493	**0.9599**	0.5589	0.5315	0.4695	0.4896	0.8986	0.5472	0.5294	**0.9587**
Std	0.0185	0.0011	0.0087	0.0145	0.0086	0.0302	0.0007	**0.0012**	0.0187	0.0012	0.0197	0.0152	0.0088	0.0322	0.0007	**0.0012**

Table 3. The index values of the segmentation results of our model and the comparison models for different initial contours.

difference between the related models, we choose several images which are downloaded from the website [2] in Figure 6. The segmentation results marked in red on the image are those of the proposed model, and those marked in green are the ground truth in the first column. To further check the robustness of our proposed model to the initial contours, we select three different initial contours for experiments to obtain the final segmentation results. The contours are inside the segmentation target, intersect with the segmentation target and outside the segmentation target. The segmentation results marked in red are the segmentation results of the proposed model and the comparison model. The WBHMS model, ICTM model, LIC model, L1PS model and DEMCV model are affected by areas with brighter edges. The CVE model can segment the focal area, but due to the unclear boundary of the focal area, the model cannot obtain accurate segmentation. Obviously, whether it is from the quantitative indicators as shown in Table 3 or the visualization results as shown in Figure 6, we can see that the proposed model has good segmentation results. The closer the values of these metrics are to 1, the closer the segmentation results are to the standard segmentation results, i.e., the closer

[2]https://www.kaggle.com/datasets/mateuszbuda/lgg-mri-segmentation

the model segmentation results are to the ground truth of segmentation, the better the segmentation performance of the algorithm. Especially, compared to our proposed model, other models obviously suffer from under-segmentation and over-segmentation. The main reason is that the hybrid bias field correction method in our proposed model can effectively improve the contrast between skull and tumor, which can result in more robust segmentation results.

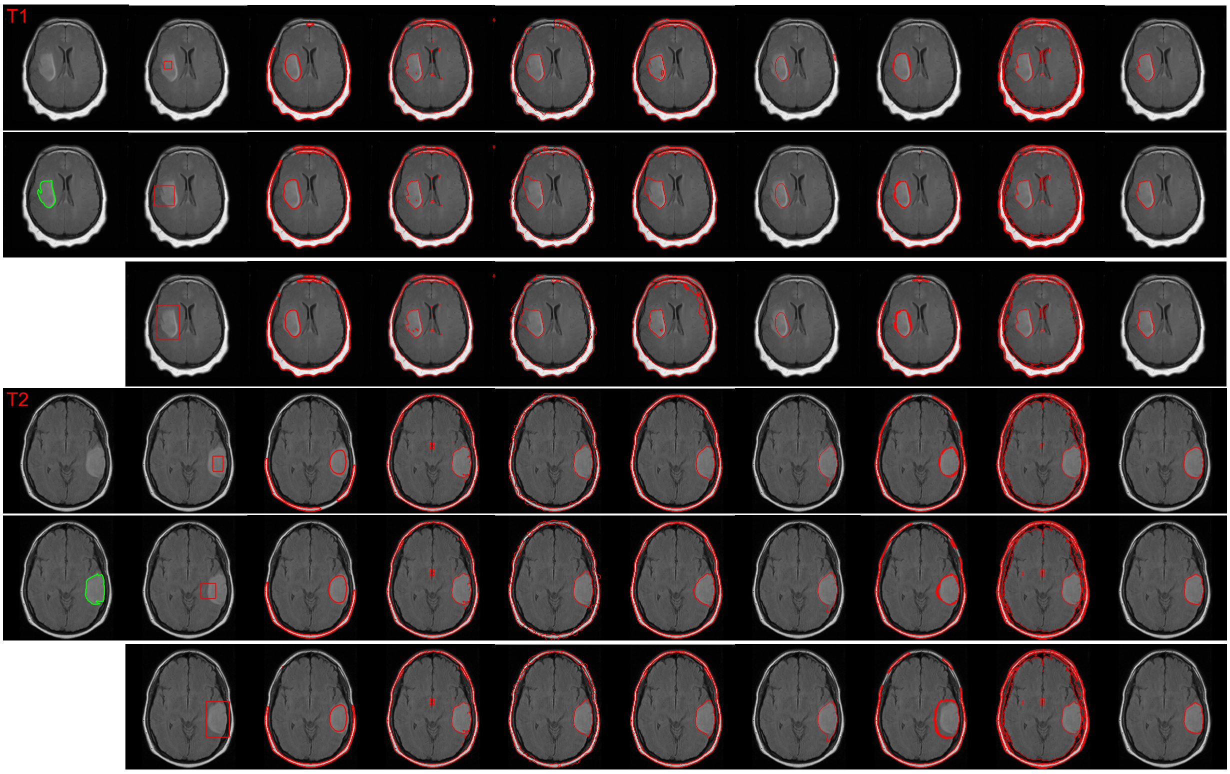

(a) Image (b) Contour (c) WBHMS (d) ICTM (e) LIC (f) L1PS (g) CVE (h) AWCA (i) DEMCV (j) OURS

Figure 6. Segmentation results of our model and comparative models in MRI brain images are shown. Three states of initial contour and region of interest.

	M1	M2	M3	M4	M5	M6	Mean	Std
JS	0.9498	0.8608	0.9277	0.6650	0.8789	0.9260	0.8680	0.0957
Accuracy	0.9984	0.9987	0.9998	0.9995	0.9989	0.9997	0.9992	0.0005
F1-score	0.9742	0.9252	0.9625	0.7988	0.9355	0.9616	0.9263	0.0594
κ	0.9734	0.9245	0.9624	0.7986	0.9350	0.9614	0.9259	0.0594

Table 4. The index values of the segmentation results of the model in MRI images.

The research on real medical images has more significant meanings than simulated images. To this end, we choose six real MRIs from the Department of Radiation Oncology of the Afliated Cancer Hospital of Zhengzhou University, where the ROI are labeled by an experienced doctor and these images are also approved by the Medical Ethics Committee of the Afliated Cancer Hospital of Zhengzhou University. The original images and ROI are shown in the first two columns of Figure 7. Here we only consider to use our proposed model to segment these images. The segmentation results marked in red on the left side of the image are our proposed model, and those marked in green are the ground truth. Since the area of the lesion is very small, we perform a local magnification to show it. For relatively small lesions, our model can still achieve good segmentation results. The relevant indicator values are shown in Table 4. It is obviously that our proposed method can efficiently segment the ROI from these real images.

To compare the CPU time, we randomly select two images from the experimental data such as natural image #1 from Figure 2 and medical image T1 from Figure 6 and the related data are arranged in Table 5. Obviously, the

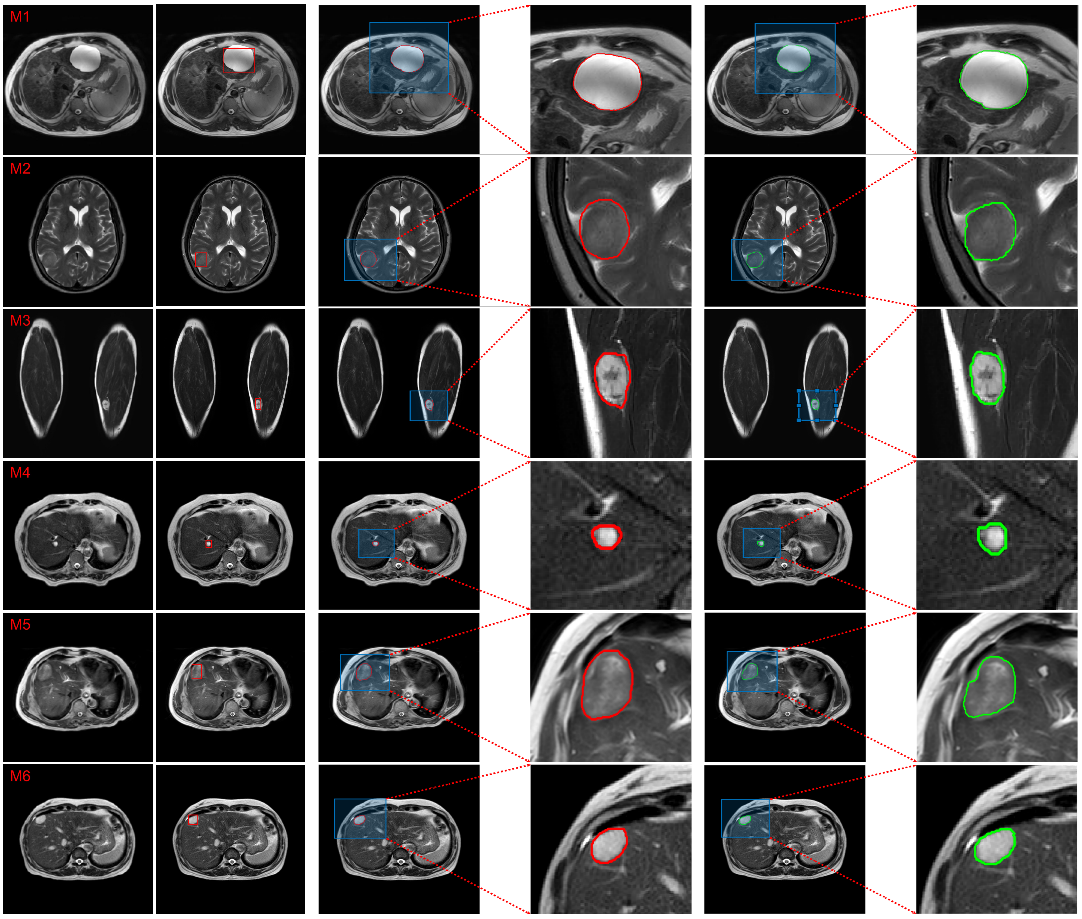

Figure 7. Segmentation results of our model in MRI images are shown. M1-M6 are the original image.

DEMCV model has the shortest runtime, but it has poor segmentation performance. However, although the CPU running time of the AWCA model is much smaller than our model, the segmentation performance of our proposed model ranks first in terms of JS, F1-score, Accuracy, and κ-coefficient values. Although the CVE model also takes a very short time, its segmentation effect is not very good. Due to the complex calculation, the ICTM has a high time consumption. Based on the above analysis, our proposed model has overwhelming advantages compared with the other seven classical models.

	WBHMS		ICTM		LIC		L1PS		CVE		AWCA		DEMCV		OURS	
#1	10	4.00s	22	15.27s	12	4.42s	20	1.71s	75	1.16s	8	0.50s	6	0.36s	70	2.00s
T1	20	3.62s	6	5.26s	12	4.30s	42	4.28s	35	0.60s	20	1.20s	10	0.75s	100	2.24s
Mean	15	3.81s	14	10.27s	12	4.36s	31	3.00s	55	0.88s	14	0.85s	8	**0.56s**	85	2.12s

Table 5. The number of iterations and CPU time (in seconds) of natural image #1 and medical image T1.

5. Conclusion

This paper proposed a hybrid bias field correction model for the intensity inhomogeneous segmentation problem. By combining the multiplicative bias field and the additive bias field, the information on the weak edge and the intensity inhomogeneity can be captured and the segmentation region in the proposed model can be described effectively. In order to efficiently solve the proposed model, we used the alternating direction method to transform the original problem into several easily solvable subproblems. Moreover, we discussed the mathematical properties of the proposed model and the corresponding algorithm. Experimental comparisons for segmenting datasets and benchmarking on several data of natural images and medical images demonstrated the improved robustness and the stability of the proposed model over several existing state-of-the-art segmentation models. However, the method proposed in this paper requires too many parameters to be adjusted, and we subsequently consider improving it.

Acknowledgements

This work was partially supported by Scientific and Technological Project in Henan Province (Nos. 212102210511, 222102310015), Natural Science Foundation of Henan Province (No.202201362), Medical Science and Technology Project in Henan Province (No. SBGJ202102056), Science and Technology Major Project of Henan Province (No. 221100310200), Natural Science Foundation of China (No. 12071345). The authors also thank the anonymous referees for both the careful reading of their manuscript and the very helpful comments and suggestions.

Author contributions

Authors (Zhenyan Guan and Yue Li): Numerical implementations and write the original draft; (Zhi-Feng Pang and Ke Chen): Theoretical analysis and guide, methodology and writing; (Hong Ge): Data labeled. All authors participated in data interpretation and helped draft the manuscript. All authors read and approved the final manuscript.

Conflict of interest

The authors declare no conflict of interest.

Appendix

Proof of Theorem 3.2.

Proof. To the subproblems (20) and (27), according to Algorithm 1, we have the following formulas of the subproblems for all the variables. All mentioned values of i in the following equations: $i = 1, 2$.

$$\left\{\begin{aligned}
&\left(c_i^{k+1}-c_i^k\right)\int_\Omega \left(b_1^k\right)^2 \mathrm{dx} = \int_\Omega b_1^k\left(I-b_2^k-p_i^k+\frac{\xi_i^k}{r}\right)\mathrm{dx} - c_i^k\int_\Omega\left(b_1^k\right)^2\mathrm{dx},\\
&\left[-2\alpha\Delta+2\nu+r\sum_{i=1}^{2}\left(c_i^{k+1}\right)^2\right]\left(b_1^{k+1}-b_1^k\right) = r\sum_{i=1}^{2}c_i^{k+1}\left(I-p_i^k-b_2^k+\frac{\xi_i^k}{r}\right)\\
&\qquad\qquad\qquad\qquad + 2\nu\mathcal{I} - \left[-2\alpha\Delta+2\nu+r\sum_{i=1}^{2}\left(c_i^{k+1}\right)^2\right]b_1^k,\\
&\left(2r\mathcal{I}-2\beta\Delta\right)\left(b_2^{k+1}-b_2^k\right) = r\sum_{i=1}^{2}\left(I-p_i^k-b_1^{k+1}c_i^{k+1}+\frac{\xi_i^k}{r}\right) - \left(2r\mathcal{I}-2\beta\Delta\right)b_2^k,\\
&\left(2\lambda u^k+r\right)\left(p_1^{k+1}-p_1^k\right) = r\left(I-b_1^{k+1}c_1^{k+1}-b_2^{k+1}\right)+\xi_1^k-\left(2\lambda u^k+r\right)p_1^k,\\
&\left[2\lambda\left(1-u^k\right)+r\right]\left(p_2^{k+1}-p_2^k\right) = r\left(I-b_1^{k+1}c_2^{k+1}-b_2^{k+1}\right)+\xi_2^k-\left[2\lambda\left(1-u^k\right)+r\right]p_2^k.
\end{aligned}\right. \tag{34}$$

and

$$\begin{cases} \tau\Delta\left(u^{k+1}-u^k\right) = \lambda\mathcal{S} + \tau\mathrm{div}\left(\mathbf{q}^k - \dfrac{\boldsymbol{\xi}_3^k}{\tau}\right) - \tau\Delta u^k + \partial\Gamma_{\mathcal{D}}(u), \\ \mathbf{q}^{k+1} - \mathbf{q}^k = \mathrm{shrinkage}\left(\nabla u^{k+1} + \dfrac{\boldsymbol{\xi}_3^k}{\tau}, \dfrac{1}{\tau}\right) - \mathbf{q}^k, \\ \dfrac{1}{r}\left(\xi_i^{k+1} - \xi_i^k\right) = -\left(p_i^{k+1} - \left(I - b_1^{k+1}c_i^{k+1} - b_2^{k+1}\right)\right), \\ \dfrac{1}{\tau}(\boldsymbol{\xi}_3^{k+1} - \boldsymbol{\xi}_3^k) = -(\mathbf{q}^{k+1} - \nabla u^{k+1}). \end{cases} \tag{35}$$

Since $\lim\limits_{k\to\infty}(A^k - A^{k-1}) = 0$ and based the assumption, the right side of the above equalities go to zero as $k \to \infty$. Based on the assumption $\xi_i^{k+1} - \xi_i^k \to 0$ as $k \to \infty$, we have $(I - b_1^{k+1}c_i^{k+1} - b_2^{k+1}) - p_i^{k+1} \to 0$. Similarly, when $\boldsymbol{\xi}_3^{k+1} - \boldsymbol{\xi}_3^k \to 0$ as $k \to \infty$, we have $\mathbf{q}^{k+1} - \nabla u^{k+1} \to 0$, etc. Then we obtain the following equations from the optimality conditions and formulations for the subproblems of all variables. Therefore, we have the following formulas go to zero as $k \to \infty$:

$$\begin{cases} \displaystyle\int_\Omega b_1^k\left(I - b_2^k - p_i^k + \frac{\xi_i^k}{r}\right)\mathrm{dx} - c_i^k\int_\Omega (b_1^k)^2\mathrm{dx} \to 0, \\ \displaystyle r\sum_{i=1}^{2} c_i^{k+1}\left(I - p_i^k - b_2^k + \frac{\xi_i^k}{r}\right) + 2\nu\mathcal{I} - \left[-2\alpha\Delta + 2\nu + r\sum_{i=1}^{2}(c_i^{k+1})^2\right]b_1^k \to 0, \\ \displaystyle r\sum_{i=1}^{2}\left(I - p_i^k - b_1^{k+1}c_i^{k+1} + \frac{\xi_i^k}{r}\right) - (-2\beta\Delta + 2r)b_2^k \to 0, \\ r(I - b_1^{k+1}c_1^{k+1} - b_2^{k+1}) + \xi_1^k - (2\lambda u^k + r)p_1^k \to 0, \\ r(I - b_1^{k+1}c_2^{k+1} - b_2^{k+1}) + \xi_2^k - [2\lambda(1-u^k) + r]p_2^k \to 0. \end{cases} \tag{36}$$

and

$$\begin{cases} \lambda\mathcal{S} + \tau\mathrm{div}\left(\mathbf{q}^k - \dfrac{\boldsymbol{\xi}_3^k}{\tau}\right) - \tau\Delta u^k + \partial\Gamma_{\mathcal{D}}(u) \to 0, \\ \mathrm{shrinkage}\left(\nabla u^{k+1} + \dfrac{\boldsymbol{\xi}_3^k}{\tau}, \dfrac{1}{\tau}\right) - \mathbf{q}^k \to 0, \\ (I - b_1^{k+1}c_i^{k+1} - b_2^{k+1}) - p_i^{k+1} \to 0, \\ \mathbf{q}^{k+1} - \nabla u^{k+1} \to 0. \end{cases} \tag{37}$$

Let $A^* = (c_i^*, b_i^*, p_i^*, u^*, \mathbf{q}^*, \xi_1^*, \xi_2^*, \boldsymbol{\xi}_3^*)_{(i=1,2)}$ be a cluster point of the generated sequence A^k based Algorithm 1. In practice, if we have $\lim\limits_{k\to\infty}(A^k - A^{k-1}) = 0$ and a convergent sequence A^k, then the sequence converges to a KKT problem point. That is to say, the conclusion (33) is held. □

References

[1] H. Ali, N. Badshah, K. Chen, and G. AliKhan. A variational model with hybrid images data fitting energies for segmentation of images with intensity inhomogeneity. Pattern Recognition, 51:27-42, 2016.

[2] H. Ali, L. Rada, and N. Badshah. Image segmentation for intensity inhomogeneity in presence of high noise. IEEE Transactions on Image Processing, 27(8):3729-3738, 2018.

[3] S. Boyd, N. Parikh, E. Chu, B. Peleato, and J. Eckstein. Distributed optimization and statistical learning via the alternating direction method of multipliers. Foundations and Trends in Machine Learning, 3:1-122, 2011.

[4] N.B. Brás, J. Bioucas-Dias, R. Martins, and A. C. Serra. An alternating direction algorithm for total variation reconstruction of distributed parameters. IEEE Transactions on Image Processing, 21(6):3004-3016, 2012.

[5] V. Caselles, R. Kimmel, and G. Sapiro. Geodesic active contours. International Journal of Computer Vision, 22: 61-79, 1997.

[6] T. Chan and L. Vese. Active contours without edges. IEEE Transactions on Image Processing, 10(2):266-277, 2001.

[7] N. Cheng, C. Cao, J. Yang, Z. Zhang, and Y. Chen. A spatially constrained skew Student's-t mixture model for brain MR image segmentation and bias field correction. Pattern Recognition, 128:108658, 2022.

[8] Y. Duan, H. Chang, W. Huang, J. Zhou, Z. Lu, and C. Wu. The L_0 regularized mumford-shah model for bias correction and segmentation of medical images. IEEE Transactions on Image Processing, 24(11):3927-3938, 2015.

[9] L. Evans. Partial Differential Equations. American Mathematical Society, 2010.
[10] E. Fang, B. He, H. Liu, and X. Yuan. Generalized alternating direction method of multipliers: new theoretical insights and applications. Mathematical Programming Computation, 7:149-187, 2015.
[11] S. Gao, J. Yang, and Y. Yan. A local modified chan-vese model for segmenting inhomogeneous multiphase images. International Journal of Imaging Systems and Technology, 22(2):103-113, 2012.
[12] X. Guo, Y. Xue, and C. Wu. Effective two-stage image segmentation: a new non-lipschitz decomposition approach with convergent algorithm. Journal of Mathematical Imaging and Vision, 63:356-379, 2021.
[13] M. Jung. Piecewise-smooth image segmentation models with L_1 data-fidelity terms. Journal of Scientific Computing, 70:1229-1261, 2017.
[14] Z. Jin, Y. Wu, L. Min, and M. Ng. A retinex-based total variation approach for image segmentation and bias correction. Applied Mathematical Modelling, 79:52-67, 2020.
[15] M. Kass, A. Witkin, and D. Terzopoulos. Snakes:active contour models. International Journal of Computer Vision, 1:321-331, 1998.
[16] C. Li, R. Huang, Z. Ding, J. Gatenby, D. Metaxas, and J Gore. A level set method for image segmentation in the presence of intensity inhomogeneities with application to MRI. IEEE Transactions on Image Processing, 20(7):2007-2016, 2011.
[17] D. Li, S. Chen, C. Feng, W. Li, and K. Yu. Bias correction of intensity inhomogeneous images hybridized with superpixel segmentation. Biomedical Signal Processing and Control. 71(B):103207, 2022.
[18] C. Li, C. Kao, J. Gore, and Z. Ding. Implicit active contours driven by local binary fitting energy. IEEE Conference on Computer Vision and Pattern Recognition, pp:1-7, 2007.
[19] F. Li, M. Ng, and C. Li. Variational fuzzy mumford-shah model for image segmentation. SIAM Journal on Applied Mathematics, 70(7):2750-2770, 2010.
[20] C. Li, J. Gore, and C. Davatzikos. Multiplicative intrinsic component optimization (MICO) for MRI bias field estimation and tissue segmentation. Magnetic Resonance Imaging, 32(7):913-923, 2014.
[21] E. Land and J. McCann. Lightness and retinex theory. Journal of the Optical Society of America, 61:1-11, 1971.
[22] Z. Liu, S. Wali, Y. Duan, H. Chang, C. Wu, and X.C. Tai. Proximal ADMM for Eulers elastica based image decomposition model. Numerical Mathematics: Theory, Methods and Applications, 12: 370-402, 2018.
[23] N. Mahata, S. Kahali, S. Adhikari, and J. Sing. Local contextual information and gaussian function induced fuzzy clustering algorithm for brain MR image segmentation and intensity inhomogeneity estimation. Applied Soft Computing, 68:586-596, 2018.
[24] H. Min, L. Xia, J. Han, X. Wang, et al. A multi-scale level set method based on local features for segmentation of images with intensity inhomogeneity. Pattern Recognition, 91:69-85, 2019.
[25] L. Min, Q. Cui, Z. Jin, and T. Zeng. Inhomogeneous image segmentation based on local constant and global smoothness priors. Digital Signal Processing, 111:102989, 2021.
[26] M. Mazurowski, K. Clark, N. Czarnek, et al. Radiogenomics of lower-grade glioma: algorithmically-assessed tumor shape is associated with tumor genomic subtypes and patient outcomes in a multi-institutional study with the cancer genome atlas data. Journal of Neuro-Oncology, 133(1):27-35, 2017.
[27] A.A. Memon, S. Soomro, M.T. Shahid, et al. Segmentation of intensity corrupted medical images using adaptive weight-based hybrid active contours. Computational and Mathematical Methods in Medicine, 6317415, 2020.
[28] Y. Niu, J. Cao, L. Liu, and H. Guo. A novel acm for segmentation of medical image with intensity inhomogeneity. The 2nd IEEE International Conference on Computational Intelligence and Applications (ICCIA), 308-311, 2017.
[29] M. Powell. Approximation Theory and Methods. Cambridge: Cambridge University Press, 1981.
[30] Z.F. Pang, M. Geng, L. Zhang, Y. Zhou, et al. Adaptive weighted curvature-based active contour for ultrasonic and 3T/5T MR image segmentation. Signal Processing, 205:108881, 2023.
[31] H. Sun, X. Tai, and J. Yuan. Efficient and convergent preconditioned ADMM for the Potts models. SIAM Journal on Scientific Computing, 43(B):455-478, 2021.
[32] S. Soomro, A. Munir, and K. Choi. Hybrid two-stage active contour method with region and edge information for intensity inhomogeneous image segmentation. PloS One, 13:e0191827, 2018.
[33] S. Saman and S. Narayanan. Active contour model driven by optimized energy functionals for mr brain tumor segmentation with intensity inhomogeneity correction. Multimedia Tools and Applications, 80:21925-21954, 2021.
[34] B. Subudhi, T. Veerakumar, S. Esakkirajan, and A. Ghosh. Context dependent fuzzy associated statistical model for intensity inhomogeneity correction from magnetic resonance images. IEEE Journal of Translational Engineering in Health and Medicine, 7:1-9, 2019.
[35] V. Venkatesh, N. Sharma, and M. Singh. Intensity inhomogeneity correction of mri images using inhomonet. Computerized Medical Imaging and Graphics, 84:101748, 2020.
[36] L. Vese and T. Chan. A multiphase level set framework for image segmentation using the mumford and shah model. International Journal of Computer Vision, 50:271-293, 2002.
[37] T. Wu, X. Gu, Y. Wang, and T. Zeng. Adaptive total variation based image segmentation with semi-proximal alternating minimization. Signal Processing, 183:108017, 2021.
[38] X. Wang, D. Huang, and H. Xu. An efficient local chan-vese model for image segmentation. Pattern Recognition, 43:603-618, 2010.
[39] D. Wang, H. Li, X. Wei, and X. Wang. An efficient iterative thresholding method for image segmentation. Journal of Computational Physics, 350:657-667, 2017.
[40] R. Wang, T. Lei, R. Cui, B. Zhang, H. Meng, and A. Nandi. Medical image segmentation using deep learning:a survey. IET Image Processing, 16(5):1243-1267 2022.
[41] G. Weng, B. Dong, and Y. Lei. A level set method based on additive bias correction for image segmentation. Expert Systems with Applications, 185:115633, 2021.
[42] Y. Wu, M. Li, Q. Zhang, and Y. Liu. A retinex modulated piecewise constant variational model for image segmentation and bias correction. Applied Mathematical Modelling, 54:697-709, 2018.
[43] B. Wahlberg, S. Boyd, M. Annergren, and Y. Wan. An ADMM algorithm for a class of total variation regularized estimation problems. IFAC Proceedings Volumes, 45(16):83-88, 2012.

[44] Y. Wang, W. Yin, and J. Zeng. Global convergence of ADMM in nonconvex nonsmooth optimization. Journal of Scientific Computing, 78(1): 29-63, 2019.

[45] Y. Yang, Q. Zhong, Y. Duan, and T. Zeng. A weighted bounded hessian variational model for image labeling and segmentation. Signal Processing, 173:107564, 2020.

[46] H. Yu, F. He, and Y. Pan. A novel segmentation model for medical images with intensity inhomogeneity based on adaptive perturbation. Multimedia Tools and Applications, 78:11779-11798, 2019.

[47] S. Yan, J. Liu, H. Huang, and X. Tai. A dual EM algorithm for TV regularized Gaussian mixture model in image segmentation. Inverse Problems & Imaging, 13(3):653-677, 2019.

[48] K. Zhang, L. Zhang, K. Lam, and D. Zhang. A level set approach to image segmentation with intensity inhomogeneity. IEEE Transactions on Cybernetics, 46(2):546-557, 2015.

[49] W. Zhu, X. Tai, and T. Chan. Image segmentation using eulers elastica as the regularization. Journal of Scientific Computing, 57:414-438, 2013.

[50] D. Zosso, J. An, J. Stevick, N. Takaki, et al. Image segmentation with dynamic artifacts detection and bias correction. Inverse Problems and Imaging, 11(3):577-600, 2017.